PHYSICAL REVIEW B VOLUME 24, NUMBER 10 15 NOVEMBER 1981

Dispersion relations in graphite intercalation compounds: Phonon dispersion curves

S. Y. Leung*
Department of Electrical Engineering and Computer Science and Center for Materials Science and Engineering, Massachusetts Institute of Technology, Cambridge, Massachusetts 02139

G. Dresselhaus
Francis Bitter National Magnet Laboratory, Massachusetts Institute of Technology, Cambridge, Massachusetts 02139

M. S. Dresselhaus
Department of Electrical Engineering and Computer Science and Center for Materials Science and Engineering, Massachusetts Institute of Technology, Cambridge, Massachusetts 02139

(Received 28 August 1980; revised manuscript received 9 April 1981)

A phenomenological model based on staging periodicity and in-plane superlattice symmetry is developed for the phonon dispersion relations of graphite intercalation compounds, analogous to the formalism developed for the electronic dispersion relations. The formalism, based on the zone folding of the graphite dynamical matrix required by symmetry, gives with a minimum number of parameters the only available calculation for the phonon dispersion relations for high-stage compounds. Specific application of the model to a $C_{2n}X$ structure yields results in good agreement with the stage dependence of the lattice mode spectra, indicating that the staging periodicity is the dominant effect in these compounds. Implications on the velocity of sound, second-order Raman spectrum, and specific-heat measurements are discussed.

I. INTRODUCTION

Graphite intercalation compounds are formed by insertion of foreign species, the intercalant, in between layers of carbon atoms, whereby an ordered structure (both c axis and possibly in plane) is formed. Over the last few years, a great many experimental results concerning the lattice dynamics of these compounds have been accumulated. There is, however, no general theoretical model for the lattice dynamics of compounds of arbitrary stage. In this paper, we apply a phenomenological model based on the symmetry imposed by the intercalation process to calculate the phonon dispersion relations. The same conceptual approach and basic formalism was previously used to calculate the electronic despersion relations.[1,2]

The following important results relevant to lattice dynamics have emerged from Raman and infrared measurements on graphite intercalation compounds and our model for the phonon dispersion relations must account for these observations. (1) Only a small number of lattice modes are observed by Raman and infrared spectroscopy. (2) Of the modes that *are* observed, almost all are very similar to those for graphite. (3) A frequency splitting of the high frequency E_{2g_2} and E_{1u} lattice modes (≈ 1600 cm^{-1}) into graphite bounding and interior layer modes is found.[3-5] (4) For the Raman-active E_{2g_2} mode, this splitting in the limit of infinite stage is larger for the donor compounds (~ 35 cm^{-1}) than for the acceptor compounds (~ 20 cm^{-1}).[5-8] (5) The E_{2g_2} mode frequency is stage dependent, and is upshifted for acceptors and downshifted for donor compounds as a function of increasing intercalant concentration.[5-8] (6) For stage-1 graphite intercalation compounds, no infrared-active modes have been observed, and likewise for stage-2 alkali metal compounds with the intercalants K, Rb, and Cs.[9] (7) For the stage-1 alkali-metal compounds with K, Rb, and Cs, an anomalous behavior is found in the Raman spectra. Instead of a sharp graphitic mode near 1600 cm^{-1}, two anomalous features are observed,[3,10,11] consist-

ing of a broad Breit-Wigner line peaking near 1500 cm^{-1}, and a sharp phonon mode structure near ~ 570 cm^{-1}. (8) The broad feature near 1500 cm^{-1} has been explained by Eklund and Subbaswammy[12] in terms of a coupling of the discrete E_{2g_2} graphitic mode to a frequency-dependent phonon continuum, while Miyazaki *et al.*[13] have interpreted this structure as due to a coupling between three discrete phonon modes and a continuum of electronic states. (9) The sharp structure in the stage-1 Raman spectra for C_8K, C_8Rb, and C_8Cs near ~ 570 cm^{-1} has been identified[10,11] as due to an M-point graphite phonon mode, folded into the Γ point of the Brillouin zone for a (2×2) superlattice, though others[14] have attributed the observed structure to peaks in the phonon density of states. (10) No measurable leakage due to intercalation is observed between the Raman and infrared spectra, implying the preservation of the parity selection rules for graphite intercalation compounds, though inversion symmetry is not formally a symmetry element of the space group. (11) The only internal mode specific to the intercalant that has been studied in detail is that for the graphite-Br_2 system,[15] by exploiting the resonant enhancement process to make the signals observable.

Other experimental investigations relevant to the lattice dynamics of intercalated graphite include inelastic neutron scattering experiments[16–19] and heat capacity measurements.[20–22] In the case of the inelastic neutron scattering experiments, the published data are scanty, with no information yet available on the stage dependence of the acoustic branches for any intercalant. From the specific-heat data,[20–22] Debye temperatures have been deduced and for the case of C_8Cs and C_8Rb, specific-heat anomalies have been identified with an Einstein temperature.[22]

Full lattice dynamical calculations for the phonon spectrum of graphite intercalation compounds have been sparse, and limited to the first-stage graphite alkali-metal compounds.[23] This calculation was based on a previous calculation by Maeda *et al.* on pristine graphite,[24] with eight force constants, and the extension of the Maeda model to C_8K and C_8Rb by Horie *et al.* employed ten force constants.[23] The Horie calculations show a large number of phonon modes (54 Γ point normal modes) mainly due to zone folding of the in-plane 2×2 superlattice. These modes, however, have not yet been observed experimentally, perhaps because of a lack of sufficient crystal perfection in these stage-1 compounds. Horie *et al.*[23] have also compared their first-principles calculation to a simple in-plane zone folding of the graphite phonon dispersion relations, showing that the major features of the phonon dispersion curves arise from zone folding of the graphite dispersion curves, rather than from perturbations associated with intercalation.

To account for the experimental observations relevant to the lattice dynamics for graphite intercalation compounds, a zone-folding model for the phonon dispersion relations is here developed which is valid for any intercalant and any stage. A preliminary and brief account of this model which takes the symmetry of graphite as the approximate symmetry of the intercalation compound has been previously presented.[7,25] The model is based on k_z-axis zone folding of the graphite dynamical matrix, consistent with the observed c-axis symmetry, in a manner analogous to that used to obtain the electron dispersion relations.[1,2] In Sec. II the lattice dynamics of graphite relevant to the model is presented. In Sec. III we extend the calculation to graphite intercalation compounds using a k_z-axis zone-folding model and giving sufficient details so that the calculation can be applied to the analysis of experimental data. In Sec. IV results of the calculation are discussed, and in Sec. V, further work and extensions to treat specific compounds are indicated.

II. LATTICE DYNAMICS OF GRAPHITE

Graphite crystallizes into a structure with D_{6h}^4 symmetry with 4 atoms per unit cell (see Fig. 1), which gives rise to 12 branches of the phonon modes which have Γ point symmetries $2A_{2u}+2E_{1u}+2E_{2g}+2B_{1g}$. These frequencies are identified by infrared spectroscopy,[26–28] first-order Raman spectroscopy,[26,29,30] and inelastic neutron diffraction measurements.[31,32]

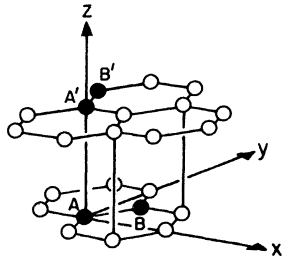

FIG. 1. Structure of hexagonal graphite showing the A, B, A', and B' atoms, and their positions with respect to the Cartesian coordinates x,y,z.

A number of models, all based on the Born—von Kármán formalism, have been reported.[24,32–37] Of the various models, the one which provides a reasonable fit to presently available experimental data is that due to Maeda *et al.*[24] and for this reason, our calculations for intercalated graphite are based on the Maeda model for pristine graphite. It should, however, be noted that the Maeda model[24] does not fit the second-order Raman data in detail, so that further refinements to the Maeda model for graphite will be necessary.

In the Maeda model, interactions up to second-nearest-neighbor in plane and first-neighbor out of plane are considered. The anisotropic properties of graphite are taken into account by two tangential force constants: one responsible for changing the bond angle within a layer and the other responsible for displacements perpendicular to the layer. The off-diagonal shear components of the force-constant matrix are assumed to be zero even though these components are allowed by symmetry. The eight force constants used in this model are listed in Table I.

III. FORM OF THE DYNAMICAL MATRIX FOR GRAPHITE INTERCALATION COMPOUNDS

According to the theory of lattice dynamics in the harmonic approximation, the dynamical matrix $D_{\alpha\beta}(\kappa\kappa' \mid \vec{k})$ is defined[38] in terms of the matrix elements $\phi_{\alpha\beta}(l\kappa;l'\kappa')$ of the force-constant matrix $\tilde{\phi}(l\kappa;l'\kappa')$ by

$$D_{\alpha\beta}(\kappa\kappa' \mid \vec{k})=(M_\kappa M_{\kappa'})^{-1/2}\sum_{l,l'}\phi_{\alpha\beta}(l\kappa;l'\kappa')\exp\{-i\vec{k}\cdot[\vec{r}(l\kappa)-\vec{r}(l'\kappa')]\}\ , \tag{1}$$

where $l\kappa$ denotes the κth atom in the lth unit cell, and $\alpha\beta$ denotes the Cartesian components. The summation in Eq. (1) is over neighbor distances which are conveniently found by calculating $\vec{r}(l\kappa)-\vec{r}(l'\kappa')$. The relation between the force-constant matrix elements $\phi_{\alpha\beta}(l\kappa;l'\kappa')$ of Eq. (1) and the force constants of Maeda *et al.*[24] (Table I) is given in Appendix A. Imposing the symmetry conditions and infinitesimal translational and rotational invariance, the following conditions between the force-constant matrices must be satisfied:

$$\phi_{\alpha\beta}(l\kappa;l'\kappa')=\phi_{\beta\alpha}(l'\kappa';l\kappa) \tag{2}$$

and

$$\sum_{l'\kappa'}\phi_{\alpha\beta}(l\kappa;l'\kappa')=0\ , \tag{3}$$

where Eq. (2) follows from the mathematical definition of the force constants, and Eq. (3) preserves the center of mass. The use of crystal symmetry results in the transformation of the force-constant matrices

$$\phi_{\alpha\beta}(l''\kappa'';l'''\kappa''')=\sum_{\zeta,\nu}S_{\alpha\zeta}S_{\beta\nu}\phi_{\zeta\nu}(l\kappa;l'\kappa')\ , \tag{4}$$

where $S_{\beta\nu}$ are the matrix representations of the symmetry operations of the space group. If the symmetry operations either leave the sites fixed $(l''\kappa'')=(l\kappa)$ and $(l'''\kappa''')=(l'\kappa')$, or interchange them $(l''\kappa'')=(l'\kappa')$ and $(l'''\kappa''')=(l\kappa)$, then the above conditions Eqs. (2)—(4) give the independent, nonzero elements of the force-constant matrices, which are tabulated explicitly in Ref. 46.

The dynamical matrix written in Eq. (1) is in the most general form. Applying the symmetry constraints of Eqs. (2)—(4) results in the formation of linear combinations of the exponential factors which transform as irreducible representations of the space group. These linear combinations of plane waves define the symmetrized Fourier functions $F^{\Gamma_i}(\vec{l},\vec{\xi})$ and the corresponding combination of force constants defines the Fourier coefficients or

TABLE I. Force constants[a] of hexagonal graphite.

$\phi_r^{(1)}$	3.066
$\phi_{ti}^{(1)}$	2.810
$\phi_{to}^{(1)}$	0.8561
$\phi_r^{(2)}$	1.363
$\phi_{ti}^{(2)}$	−0.5269
$\phi_{to}^{(2)}$	−0.1421
$\hat{\phi}_r^{(1)}$	0.0579
$\hat{\phi}_t^{(1)}$	0.00718

[a]The values of the force constants in units of (10^5 dyn/cm) are from Maeda *et al.* (Ref. 24). The subscript r denotes a radial force constant and t a tangential force constant, with ϕ_{to} and ϕ_{ti} associated, respectively, with a change in bond angle and a c-axis displacement. The out-of-plane force constants $\hat{\phi}^{(n')}$ are distinguished from the in-plane force constants $\phi^{(n)}$, where n refers to the nth neighbor in-plane distance and n' to the n'th neighbor out-of-plane distance. We note that Maeda *et al.* (Ref. 24) used the superscript notation ϕ^{int} to denote the $\hat{\phi}^{(1)}$ terms given in the above table.

Fourier parameters. The relations of the Fourier functions $F^{\Gamma_i}(\vec{l},\vec{\xi})$ to the plane waves are listed in Table II. Listed in Table III are the relations of the in-plane Fourier parameters $a^{A_{1g}}_{\alpha\beta}(hk0,\nu)$ to a linear combination of the in-plane and out-of-plane Maeda force constants $\phi^{(i)}$ and $\hat{\phi}^{(i)}$ for graphite (see Table I).

The dynamical matrix in the site representation for graphite with four distinct atoms per unit cell A, B, A', and B' is a 12×12 matrix of the form

$$D_g=\begin{bmatrix} D_{AA} & D_{AB} & D_{AA'} & D_{AB'} \\ D^{\dagger}_{AB} & D_{BB} & D_{BA'} & D_{BB'} \\ D^{\dagger}_{AA'} & D^{\dagger}_{BA'} & D_{A'A'} & D_{A'B'} \\ D^{\dagger}_{AB'} & D^{\dagger}_{BB'} & D^{\dagger}_{A'B'} & D_{B'B'} \end{bmatrix}, \tag{5}$$

where the $D_{\alpha\beta}$ are 3×3 matrices coupling atoms α and β, and are subject to the symmetry-imposed constraints given above and resulting in the following relations between matrix elements. Firstly we have

$$(D_{\beta\alpha})_{ji}=(D_{\alpha\beta})^{*}_{ij} \tag{6}$$

for $\alpha,\beta=A, B, A', B'$ and $i,j=x+iy, x-iy, z$. Additional constraints on the off-diagonal terms of the dynamical matrix are the following:

$$(D_{\alpha\alpha})_{ij}=(D_{\beta\beta})_{ij} \tag{7}$$

for $i\neq j$ and, either $\alpha=A'$, $\beta=A$, or $\alpha=B'$, $\beta=B$, or $\alpha=B$, $\beta=A$.

Using the Fourier functions $F^{\Gamma_i}(\vec{l},\vec{\xi})$ and Fourier parameters $a^{\Gamma_i}_{\alpha\beta}(\vec{l},\nu)$ listed in Tables II and III, the independent matrix elements of the dynamical matrix are obtained and are tabulated in Appendix B. With the matrix elements given in Appendix B, the phonon dispersion relations for graphite, given by Maeda *et al.*,[24] are reproduced.

To take into account the c-axis periodicity imposed by the staging superlattice, the dynamical matrix for graphite is zone folded along k_z to generate the dynamical matrix of the intercalation compound. For the graphite intercalation compounds, the c-axis superlattice which results from staging is well documented.[39] On the other hand, experimental results on the lattice mode spectra for these compounds show, except for stage 1, no observable dependence on in-plane structure.[40] Moreover, most intercalation compounds do not have in-plane intercalate layer ordering that is commensurate with the graphite host, so that few intercalation compounds exhibit an in-plane superlattice.[40] Hence, we start our modeling of the lattice dynamics of graphite intercalation compounds by the introduction of k_z-axis zone folding.

For our model calculations, we distinguish between odd and even stage compounds because the crystallographic inequivalence of the A,B layers in pristine graphite gives a one and two intercalate layer c-axis periodicity for odd and even stages, respectively. The Brillouin zone is then respectively $(n+1)/2$ and $(n+1)$ times smaller than graphite for odd and even stages in the intercalation compounds. The inverse scaling relation likewise ap-

TABLE II. Symmetrized Fourier functions for hexagonal graphite.[a]

Representation: Γ_i	Fourier function[b]: $F^{\Gamma_i}(\vec{l},\vec{\xi})$
A_{1g}	$[C^0(l_1,l_2)+C^0(l_2,l_1)]\cos(\pi l_3\xi_3)$
A_{2g}	$[C^0(l_1,l_2)-C^0(l_2,l_1)]\cos(\pi l_3\xi_3)$
B_{1g}	$[S^0(l_1,l_2)-S^0(l_2,l_1)]\sin(\pi l_3\xi_3)$
B_{2g}	$[S^0(l_1,l_2)+S^0(l_2,l_1)]\sin(\pi l_3\xi_3)$
E_{1g}	$\begin{cases}[S^1(l_1,l_2)+\Omega S^1(l_2,l_1)]\sin(\pi l_3\xi_3)\\ i\,[S^1(l_1,l_2)-\Omega S^1(l_2,l_1)]\sin(\pi l_3\xi_3)\end{cases}$
E_{2g}	$\begin{cases}[C^1(l_1,l_2)+\Omega C^1(l_2,l_1)]\cos(\pi l_3\xi_3)\\ i\,[C^1(l_1,l_2)-\Omega C^1(l_2,l_1)]\cos(\pi l_3\xi_3)\end{cases}$
A_{1u}	$i\,[C^0(l_1,l_2)-C^0(l_2,l_1)]\sin(\pi l_3\xi_3)$
A_{2u}	$i\,[C^0(l_1,l_2)+C^0(l_2,l_1)]\sin(\pi l_3\xi_3)$
B_{1u}	$i\,[S^0(l_1,l_2)+S^0(l_2,l_1)]\cos(\pi l_3\xi_3)$
B_{2u}	$i\,[S^0(l_1,l_2)-S^0(l_2,l_1)]\cos(\pi l_3\xi_3)$
E_{1u}	$\begin{cases}[S^1(l_1,l_2)+\Omega S^1(l_2,l_1)]\cos(\pi l_3\xi_3)\\ i\,[S^1(l_1,l_2)-\Omega S^1(l_2,l_1)]\cos(\pi l_3\xi_3)\end{cases}$
E_{2u}	$\begin{cases}[C^1(l_1,l_2)+\Omega C^1(l_2,l_1)]\sin(\pi l_3\xi_3)\\ i\,[C^1(l_1,l_2)-\Omega C^1(l_2,l_1)]\sin(\pi l_3\xi_3)\end{cases}$

[a]The dimensionless reciprocal-lattice vectors ξ_1, ξ_2, ξ_3 are given by $\xi_1=k_1a_0/2\pi$, $\xi_2=k_2a_0/2\pi$, and $\xi_3=k_3c_0/2\pi$, where k_1, k_2, and k_3 are given in Eq. (A3) in Appendix A.

[b]The linear combinations of exponentials using in-plane vectors are given by

$$C^j(l_1,l_2)=(\cos[2\pi(l_1\xi_1+l_2\xi_2)/3]+\Omega^j\cos\{2\pi[-l_2\xi_1+(l_1-l_2)\xi_2]/3\}+\Omega^{2j}\cos\{2\pi[(l_2-l_1)\xi_1-l_1\xi_2]/3\})/6\,,$$

$$S^j(l_1,l_2)=(\sin[2\pi(l_1\xi_1+l_2\xi_2)/3]+\Omega^j\sin\{2\pi[-l_2\xi_1+(l_1-l_2)\xi_2]/3\}+\Omega^{2j}\sin\{2\pi[(l_2-l_1)\xi_1-l_1\xi_2]/3\})/6\,,$$

in which $\Omega=\exp(2\pi i/3)$. The partners of the two functions for each of the 2-dimensional representations are the complex conjugates of the listed functions.

TABLE III. Relation of Fourier parameters to force constants for graphite.

Symmetrized parameters[a]	Maeda parameters
$a_{AA}^{A_{1g}}(000,1)$	$[(\frac{3}{2})(\phi_r^{(1)}+\phi_{ti}^{(1)})+2(\phi_r^{(2)}+\phi_{ti}^{(2)})+2\hat{\phi}_r^{(1)}]/m_C$
$a_{AA}^{A_{1g}}(000,4)$	$[3(\phi_{to}^{(1)}+2\phi_{to}^{(2)})+2\hat{\phi}_r^{(1)}]/m_C$
$a_{AA}^{A_{1g}}(300,1)$	$-3(\phi_{ti}^{(2)}+\phi_r^{(2)})/m_C$
$a_{AA}^{A_{1g}}(300,3)$	$-3[\phi_{ti}^{(2)}-\phi_r^{(2)}]/m_C$
$a_{AA}^{A_{1g}}(300,4)$	$-6\phi_{to}^{(2)}/m_C$
$a_{BB}^{A_{1g}}(000,1)$	$[(\frac{3}{2})(\phi_r^{(1)}+\phi_{ti}^{(1)})+2(\phi_r^{(2)}+\phi_{ti}^{(2)})]/m_C$
$a_{BB}^{A_{1g}}(000,4)$	$3(\phi_{to}^{(1)}+2\phi_{to}^{(2)})/m_C$
$a_{BB}^{A_{1g}}(300,1)$	$-3(\phi_{ti}^{(2)}+\phi_r^{(2)})/m_C$
$a_{BB}^{A_{1g}}(300,3)$	$-3[\phi_{ti}^{(2)}-\phi_r^{(2)}]/m_C$
$a_{BB}^{A_{1g}}(300,4)$	$-6\phi_{to}^{(2)}/m_C$
$a_{AA'}^{A_{1g}}(001,1)$	$-2\hat{\phi}_t^{(1)}/m_C$
$a_{AA'}^{A_{1g}}(001,4)$	$-2\hat{\phi}_r^{(1)}/m_C$
$a_{AB}^{A_{1g}}(120,1)$	$-[(\frac{3}{2})(\phi_r^{(1)}+\phi_{ti}^{(1)})]/m_C$
$a_{AB}^{A_{1g}}(120,3)$	$[-3(\phi_r^{(1)}-\phi_{ti}^{(1)})]/m_C$
$a_{AB}^{A_{1g}}(120,4)$	$-3\phi_{to}^{(1)}/m_C$

[a]In addition to the listed parameters, we have the identities:

$$a_{A'A}^{A_{1g}}(\vec{l},\nu)=a_{AA}^{A_{1g}}(\vec{l},\nu)\,,$$

$$a_{B'B}^{A_{1g}}(\vec{l},\nu)=a_{BB}^{A_{1g}}(\vec{l},\nu)\,,$$

$$a_{A'B}^{A_{1g}}(\vec{l},\nu)=a_{AB}^{A_{1g}}(-\vec{l},\nu)\,.$$

Parameters not listed are taken to be zero in the Maeda model.

plies to the k_z-axis reciprocal-lattice vectors.

The definition of the phonon dispersion curve $\omega(\vec{k})$ in the reduced zone gives rise to the relation

$$\omega(\vec{k})=\omega(\vec{k}+\vec{G})\,, \tag{8}$$

where $\vec{G}$ is a reciprocal-lattice vector in the new superlattice. Considering k_z-axis zone folding, we have for the smallest reciprocal-lattice vector $\vec{G}_{001}=\pi\hat{z}/(lc_0)$, where $l=(n+1)/2$ for odd stages and $l=(n+1)$ for even stages. Thus Eq. (8) under k_z-axis zone folding yields

$$\omega(\vec{k})=\omega\left[\vec{k}+\frac{\pi\hat{z}}{lc_0}\right]=\omega\left[\vec{k}+\frac{2\pi\hat{z}}{lc_0}\right]$$
$$=\cdots=\omega\left[\vec{k}+\frac{(l-1)\pi\hat{z}}{lc_0}\right]. \tag{9}$$

Therefore the k_z-axis zone-folded dynamical matrix takes the form

$$D_{ZF}(\vec{k})=\begin{bmatrix} D_g(\vec{k}) & 0 & \cdots & 0 \\ 0 & D_g\left[\vec{k}+\frac{\pi\hat{z}}{lc_o}\right] & & \vdots \\ \vdots & & D_g\left[\vec{k}+\frac{2\pi\hat{z}}{lc_0}\right] & \\ & & & \ddots \\ 0 & \cdots & & D_g\left[\vec{k}+\frac{(l-1)\pi\hat{z}}{lc_0}\right] \end{bmatrix} \tag{10}$$

in which each $D_g(\vec{k})$ block is a 12×12 graphite dynamical matrix as given by Eq. (5), and blocks of zeros are placed in the off-diagonal positions.

To consider the effect of the intercalant explicitly, the dynamical matrix is conveniently handled in the layer representation, where one can identify each layer of the compound with a specific row and/or column of the dynamical matrix. In the layer representation we can then replace a graphite layer by an intercalant layer, thereby explicitly incorporating the effect of the intercalant. The transformation to the layer representation D_L is carried out via the unitary transformation U given in Appendix C and yielding

$$D_L(\vec{k})=UD_{ZF}(\vec{k})U^{-1}\,. \tag{11}$$

The dynamical matrix in the layer representation $D_L(\vec{k})$ is then written as

$$D_L(\vec{k})=\begin{bmatrix} D_{A_0A_0} & D_{A_0B_0} & \cdots & & & \\ D^{\dagger}_{A_0B_0} & D_{B_0B_0} & D_{B_0A_1} & \cdots & & \\ \cdot & D^{\dagger}_{B_0A_1} & D_{A_1A_1} & & & \\ \cdot & & & \ddots & & \\ \cdot & & & & D_{A_lA_l} & D_{A_lB_l} \\ & & & & D^{\dagger}_{A_lB_l} & D_{B_lB_l} \end{bmatrix} \tag{12}$$

in which the matrix blocks, such as $D_{A_0A_0}$ and $D_{A_0B_0}$, etc., are $(3r\times3r)$ matrices, where r is the number of carbon atoms per unit cell, and the subscripts denote the layer indices.

Using $D_L(\vec{k})$ as the basic zone-folded graphite dynamical matrix, we can examine the effect of intercalation on the dynamical matrix $D_L(\vec{k})$ and on the phonon dispersion relations for three different cases to which our model applies: (a) zone-folded graphite, where the intercalate layer is assumed to be identical to a graphite layer, (b) the "empty intercalate layer" approximation, where the intercalate layer is replaced by an empty later (i.e., vacuum), and (c) the occupied intercalate layer approximation, where the intercalant can be a "modified graphite layer" or a specific ionic or molecular configuration which interacts with the graphite bounding layers. The dynamical matrix appropriate to the replacement of every $(n+1)$st graphite layer by an intercalate layer is written in the most general form (for odd stages) as

$$D_{GIC}=\begin{bmatrix} D_{XX} & D_{XB_0} & \cdots & & & D_{XB_l} \\ D^{\dagger}_{XB_0} & D_{B_0B_0} & D_{B_0A_1} & & & \\ \cdot & D^{\dagger}_{B_0A_1} & D_{A_1A_1} & & & \\ \cdot & & & \ddots & & \\ \cdot & & & & & \\ & & & & D_{A_lA_l} & D_{A_lB_l} \\ D^{\dagger}_{XB_l} & & & & D^{\dagger}_{A_lB_l} & D_{B_lB_l} \end{bmatrix} \tag{13}$$

and for even stages as

$$
D_{GIC}=\begin{bmatrix}
D_{XX} & D_{XB_0} & & \cdots & & & & & & D_{XB_l} \\
D_{XB_0}^{\dagger} & D_{B_0B_0} & D_{B_0A_1} & & & & & & & \\
\cdot & D_{B_0A_1}^{\dagger} & D_{A_1A_1} & & & & & & & \\
\cdot & & & & & & & & & \\
\cdot & & & \ddots & & & & & & \\
 & & & & D_{A_\mu A_\mu} & D_{A_\mu X} & & & & \\
 & & & & D_{A_\mu X}^{\dagger} & D_{XX} & D_{XA_\nu} & & & \\
 & & & & & D_{XA_\nu}^{\dagger} & D_{A_\nu A_\nu} & & & \\
 & & & & & & & \ddots & & \\
 & & & & & & & & D_{A_lA_l} & D_{A_lB_l} \\
D_{XB_l}^{\dagger} & & & & & & & & D_{A_lB_l}^{\dagger} & D_{B_lB_l}
\end{bmatrix} \tag{14}
$$

To obtain zone-folded graphite, we write $X=A_0$ in Eqs. (13) and (14) and recover the $D_L(\vec{k})$ matrix of Eq. (12). For the empty intercalate layer approximation, we set all blocks with subscript X equal to zero: $D_{XX}=\ldots D_{XB_0}=D_{XB_l}=D_{A_\mu X}=D_{XA_\nu}=0$.

In the present work, we are especially interested in an occupied intercalate layer for a generalized intercalation compound, and we consider two limiting cases explicitly: (1) The intercalate layer is a modified graphite layer where the intralayer symmetry and atomic positions are those of pristine graphite but the in-plane and out-of-plane force constants are modified, as is the atomic mass, or (2) the intercalate layer forms a commensurate $C_{2n}X$ structure for a stage n compound, with an intercalant over the center of every graphite hexagon, where again the mass and the in-plane and out-of-plane force constants are modified.

Taking the intercalant as a modified graphite layer we obtain

$$
\begin{aligned}
&D_{XG}=\eta D^0_{A_0G}\ , \\
&D_{XX}=D^0_{A_0A_0}+(\sigma-\eta)\sum_G D^0_{A_0G}(\vec{k}=0)\ , \\
&D_{gg}=D^0_{gg}+(f-\eta)\sum_g D^0_{A_0g}(\vec{k}=0)\ ,
\end{aligned} \tag{15}
$$

in which $g=B_0, A_1, B_1, \ldots, B_l$, and $D^0_{\alpha\beta}$ is the pristine graphite matrix of Eq. (5), with δ controlling the intercalant-graphite interactions, σ governing the intercalant-intercalant interaction, $f=1$ for stage 1, $f=\frac{1}{2}$ for other stages, and G denoting the graphite bounding layers. The $\vec{k}=0$ terms in Eq. (15) are required to conserve the center of mass and to obtain the acoustic branches at $\vec{k}=0$ correctly. It should be noted that in the layer representation one can also modify the force constants within the bounding graphite layer or the interactions between graphite bounding and interior layers. Preliminary analysis[18] of inelastic neutron scattering from longitudinal acoustic modes suggest a significant decrease in the bounding-interior layer graphite interaction relative to pristine graphite.

The $C_{2n}X$ structure is important for a generalized treatment of the phonon modes for intercalated graphite because it allows the formulation of the dynamical matrix in which the atomistic nature of the intercalate layer is incorporated with AXA registry. In this registry the intercalate atom or molecule is centered between two hexagons on the graphite bounding layer planes. The $C_{2n}X$ structure corresponds to a 1×1 superlattice for the intercalate layer. The cases for less dense superlattices, e.g., $\sqrt{3}\times\sqrt{3}$, 2×2, $\sqrt{7}\times\sqrt{7}$, etc., can be treated by an in-plane zone folding of the $C_{2n}X$ dynamical matrix with the subsequent removal of selected intercalate atoms or molecules. Since commensurate superlattices do not generally exist for stage $n>1$, the application of the $C_{2n}X$ structure for the modeling of intercalation compounds makes use of a distributed layer in which the mass per unit area is fit to the experimental value for the intercalate layer. Though this model overestimates the number of intercalate-related modes, the simplicity of the model makes it possible to calculate high-stage intercalation compounds without excessive computer time.

For the case of the $C_{2n}X$ structure, we modify the B atom on the A_0 layer to that of an intercalant and leave the A atom site vacant. The D_{XX}

matrix then becomes a $3r \times 3r$ matrix, where r is the number of atoms in the intercalate unit, and reflects the internal degrees of freedom for the intercalant (i.e., $r=1$ for an atomic or ionic intercalant such as K, $r=2$ for the molecular intercalant Br_2, etc). Within the $C_{2n}X$ formalism, in which the A_0 layer is modified to model the intercalate layer, the A site is eliminated, the intercalant-intercalant interaction has the same form as the in-plane graphite B-B site interaction, and the intercalant-graphite bounding layer interaction takes the same functional form as the graphite A-B' and B-B' interactions. Since the first nonvanishing out-of-plane contribution for the $C_{2n}X$ structure occurs at the second-neighbor out-of-plane distance, it is necessary to extend the calculation for graphite by Maeda *et al.*[24] to include such terms. An explicit listing of the intercalate-related matrix elements of Eqs. (13) and (14) for the $C_{2n}X$ structure is given in Appendix D for the case $r=1$ and assuming only nearest-neighbor intercalant-intercalant interactions. In Eqs. (13) and (14) we substitute $B_l=B^+$ and $B_0=B^-$ and for even stages $A_\mu=A^+$ and $A_\nu=A^-$ in the graphite-intercalate interaction terms. Also included in Appendix D are the results for stage-1 compounds, for which every graphite layer is adjacent to an intercalate layer.

To incorporate the stage dependence of the dynamical matrix in detail, we proceed to include a stage dependence of the in-plane graphite force constants for the bounding layers of the form

$$\phi=\phi_0(1+\alpha/n)\,, \tag{16}$$

where ϕ_0 is the force constant for pristine graphite and α gives the stage dependent part of the force constants, and is positive for acceptors and negative for donors. The physical basis for this stage dependence of the in-plane force constants can come from a variety of different stage dependent mechanisms, such as changes in: (1) the in-plane carbon-carbon distance (bond length) d_{C-C} of the intercalation compound from that of pristine graphite,[41–44] where d_{C-C} increases for donors and decreases for acceptors upon intercalation, (2) bond strength as a result of charge transfer,[45] and (3) the electron-phonon coupling as a result of the renormalization of the phonon modes by free carrier (plasma) effects.[46] In our calculations, the stage dependence of the out-of-plane force constants $\hat{\phi}$ were neglected for lack of experimental information. This assumption can of course be relaxed when the pertinent experimental information becomes available.

The inverse stage dependence of the E_{2g_2} mode frequencies has been associated with the measured changes in the in-plane bond length d_{C-C}. These changes in d_{C-C} have been shown to be of opposite sign for donors and acceptors and to scale as the inverse stage $1/n$. Such a functional dependence on $1/n$ is associated with a power-series expansion in the intercalate concentration. Recent theoretical calculations by Pietronero and Strässler have estimated the effect of charge transfer into the graphite from the change in the in-plane bond length.[45]

IV. RESULTS FOR THE PHONON DISPERSION RELATIONS AND DENSITY OF STATES

Based on the formalism derived in the last section, we have calculated the phonon dispersion relations of graphite intercalation compounds in four limiting cases: (1) zone-folded graphite, (2) the empty intercalate layer approximation, (3) the intercalate layer as a "modified graphite layer," and (4) the $C_{2n}X$ structure.

Results for cases (1), (2), and (3) are illustrated in Fig. 2 for a stage $n=3$ compound. Figure 2(a) shows that k_z-axis zone folding increases the number of the graphite phonon dispersion relations branches by a factor of 3 for $n=3$. As shown in Fig. 2(b), the effect of the removal of a graphite layer and the substitution of an empty intercalate layer is the removal of six phonon branches from the dispersion curves with little perturbation to the remaining branches, except that the k_z dispersion is eliminated due to the absence of any coupling across the intercalate layer. This loss of k_z dispersion is reasonable for this model in light of the increase in the separation between two graphite bounding layers because of the intervening intercalate layer. Neither the k_z-axis zone-folded graphite nor the empty intercalate layer model can account for the splitting of the high-frequency optic mode into bounding and interior layer modes.

To account for this splitting, interaction terms such as given by Eq. (16) for the modified graphite layer are included. The interaction parameters η and σ in Eqs. (15) are assumed to differ from one intercalant to another and to differ for donors relative to acceptors. Results for the phonon dispersion relations for the modified graphite layer model are shown in Figs. 2(c) and 2(d) for donors and acceptors, respectively. The main effect of the intercalant-graphite bounding layer interaction is

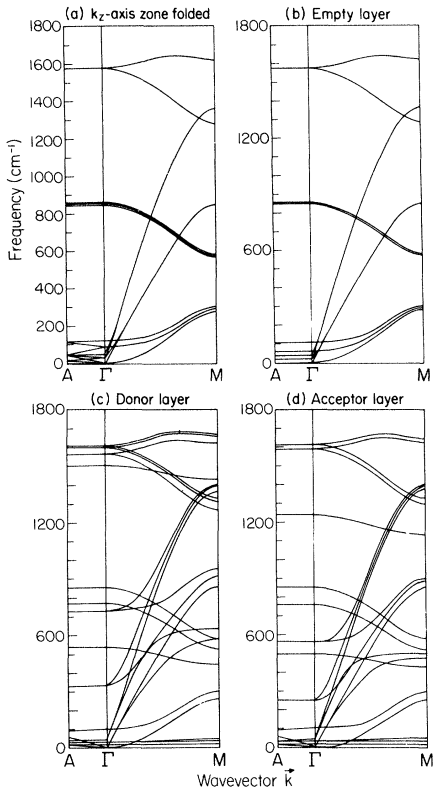

FIG. 2. Phonon dispersion curves for stage-3 graphite intercalation compounds under the following conditions: (a) k_z-axis zone-folded graphite, (b) empty intercalate layer model, (c) modified graphite layer model donor compound, and (d) modified graphite layer model acceptor compound.

the splitting of *all* the graphite optic modes into bounding and interior layer modes. This interaction also couples the intercalate mode to the low-frequency graphitic branches of the dispersion curves. The largest bounding-interior layer splitting is predicted to occur for the modes originating from the out-of-plane A_{2u} modes of graphite. In the low-frequency region, the dominant modes in the intercalation compounds show a large admixture between the graphitic and intercalant parent modes. Because of this admixture of low-frequency modes, it is only for the high-frequency optic modes that intercalant-independent shifts are observed experimentally.[7] It should, however, be noted that the intercalate mode is sensitive to the assumptions of the model, which in this case considers the intercalate layer as a modified graphite layer with the same number of atoms and symmetry as a graphite layer. This assumption must of course be modified for each intercalant to account for the proper intercalant to graphite mass ratio per unit in-plane area, and the proper intercalate in-plane symmetry.

A more realistic approach for including the effect of the intercalant is given by the $C_{2n}X$ structure, where the intercalant is assumed to be centered over a potential minimum. This corresponds to an intercalant on a B' site, an A' site unoccupied, and carbon atoms on A and B sites on the adjacent layers. In this situation the intercalant-intercalant interaction is required by symmetry to take the same form as the second-nearest-neighbor in-plane graphite-graphite interaction, except for the difference in the magnitude of the force constants (see Table IV). There are no terms at the nearest-neighbor and third-neighbor in-plane graphite distances for this structure. The intercalant-graphite interaction, on the other hand, is identical in form to the second-neighbor *out-of-plane* AB' and BB' interactions for graphite, again with different force constants. There are no terms corresponding to the nearest-neighbor out-of-plane distance. For this model it is necessary to introduce six parameters in addition to the pristine graphite parameters. These additional parameters are (a) the radial and tangential components of the intercalant-intercalant force constants (ϕ_r^{XX} and ϕ_t^{XX}), (b) the radial and tangential components of the intercalant-graphite force constants (ϕ_r^{XG} and ϕ_t^{XG}), and (c) the ratio of the intercalant mass to graphite mass ($\rho = m_X/m_C$) per unit in-plane area, and the coefficient α for the stage dependence of the graphite in-plane force constants given by Eq. (16). The intercalant-intercalant interaction parameters and the mass parameter per unit area are determined mainly by the properties of the parent intercalant. The values for the intercalant-graphite interaction parameters and for the α coefficient in Eq. (16) are adjusted to fit the experimental Raman data.

The values for the six parameters chosen for the present calculation are summarized in Table V. These parameters are chosen for a generalized donor and a generalized acceptor compound without reference to any specific intercalant or stage. The intercalant-intercalant force constants ϕ_r^{XX} and ϕ_t^{XX} are chosen to be small, as discussed below. The intercalant mass per unit area (m_X) has been taken to be equal to that for the graphite layers (m_C) or $\rho = 1$. The intercalant-graphite interaction is chosen for simplicity to have equal tangential and radial force constants (i.e., $\hat{\phi}_r^{XG} = \hat{\phi}_t^{XG} = \hat{\phi}^{XG}$). With these approximations the magnitude of $\hat{\phi}^{XG}$ has been determined by the observed

TABLE IV. Fourier parameters for the intercalant-intercalant and intercalant-graphite interactions.

Symmetrized constants	Force constants[a]
$a_{XX}^{A_{1g}}(000,1)$	$[3(\phi_r^X+\phi_{ti}^X)+3(\zeta^2\phi_t^{XG}+\epsilon^2\phi_r^{XG}+\phi_t^{XG})]/m_X$
$a_{XX}^{A_{1g}}(000,4)$	$[6\phi_{to}^X+6(\epsilon^2\phi_t^{XG}+\zeta^2\phi_r^{XG})]/m_X$
$a_{XX}^{A_{1g}}(300,1)$	$-3(\phi_{ti}^X+\phi_r^X)/m_X$
$a_{XX}^{A_{1g}}(300,3)$	$-3(\phi_{ti}^X-\phi_r^X)/m_X$
$a_{XX}^{A_{1g}}(300,4)$	$-6\phi_{to}^X/m_X$
$a_{XG}^{A_{1g}}(000,1)$	$-\frac{3}{2}(\zeta^2\phi_t^{XG}+\epsilon^2\phi_r^{XG}+\phi_t^{XG})/(m_Xm_C)^{1/2}$
$a_{XG}^{A_{1g}}(000,3)$	$-3\epsilon^2(\phi_r^{XG}-\phi_t^{XG})/(m_Xm_C)^{1/2}$
$a_{XG}^{A_{1g}}(000,4)$	$-3(\epsilon^2\phi_t^{XG}+\zeta^2\phi_r^{XG})/(m_Xm_C)^{1/2}$
$a_{XG}^{A_{1g}}(000,5)$	$-3\sqrt{2}\epsilon\zeta(\phi_r^{XG}-\phi_t^{XG})/(m_Xm_C)^{1/2}$

[a]In addition to the Maeda force constants, we introduce the intercalate mass m_X and the carbon mass m_C per unit in-plane area, and the parameters $\epsilon=(a_0/\sqrt{3})(c_0^2+a_0^2/3)^{-1/2}$, $\zeta=c_0(c_0^2+a_0^2/3)^{-1/2}$.

splitting of the graphite bounding and interior layer E_{2g_2} Raman-active modes in the limit of infinite stage (i.e., pristine graphite). The magnitude of α has been chosen to fit the dependence of the bounding layer E_{2g_2} mode frequency on reciprocal stage ($1/n$). For the values of α and ϕ^{XG} listed in Table V, the mode frequencies for bounding and interior layer modes are calculated and the results are given in Fig. 3 for acceptors as open circles and for donors as closed circles. The solid and dashed lines for the bounding layer modes are from a least-square fit to experimental data. We also note that the experimental results for the interior layer modes for the donor compounds do not show as large a shift as our calculated results.

The small magnitude of the ϕ_r^{XX} and ϕ_t^{XX} force constants reflects the fact that in a real compound the intercalants are separated by a large distance relative to the carbon-carbon nearest-neighbor distances, so that the interactions between atoms in the intercalate layer are assumed to be small compared to the interactions between the intercalant and graphite. It is further observed from the calculation that the phonon dispersion relations for the optical and acoustic graphitic modes are not sensitive to the intercalant-intercalant interaction parameter. Explicit calculations for a stage-1 compound, where the eigenfrequencies should be most

TABLE V. Values for parameters used in the lattice dynamical calculation for a generalized donor and acceptor compound.

	Donor	Acceptor
$\phi_r^{XX}(10^3$ dyn/cm)	1.0	1.0
$\phi_t^{XX}(10^2$ dyn/cm)	1.0	1.0
$\phi_r^{XG}(10^4$ dyn/cm)	2.66	1.70
$\phi_t^{XG}(10^4$ dyn/cm)	2.66	1.70
ρ	1.0	1.0
α	−0.0388	0.0378

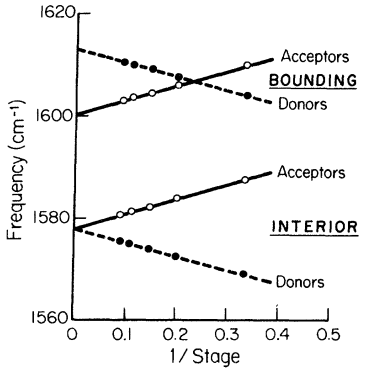

FIG. 3. Calculated mode frequencies vs reciprocal stage for graphite bounding and interior layer Raman-active E_{2g_2} lattice modes. The open circles are calculated for acceptor compounds and the solid circles for donor compounds. The constants of the model were determined to fit the experimental data of Refs. 9 and 46, and the pertinent parameters are given in Tables I and V.

sensitive to the intercalant-intercalant interaction, show no change in the mode frequencies at the Γ point and at the A point over the range of ϕ_r^{XX} values from 0 to 10^4 dyn/cm. However, at the M point a small change in the acoustic-mode frequencies is observed.[46]

For simplicity we have chosen the intercalate mass per unit in-plane area to be that of carbon, so that $\rho=1$, which is approximately valid for the $C_{12n}Cs$ structure for which $\rho=0.92$. For application to specific intercalants, the appropriate value for ρ must be included. The calculation of the dependence of the Γ-point mode frequencies on ρ shows, as expected, that the modes with the strongest dependence on ρ are the triply degenerate modes that involve mainly intercalant vibrations.[46]

With the choice of parameters shown in Table V, the phonon dispersion relations for stages 3, 5, 7, 9, and 11 acceptor and donor compounds have been calculated and the results along ΓM are shown in Fig. 4. In previously published phonon dispersion relations for the stage-1 compounds,[25] the curves are found to be qualitatively different from those for the higher-stage compounds. Furthermore, the phonon dispersion relations for stages 3, 5, 7, 9, and 11 are almost identical, except for the splitting of the lowest-frequency branches. Comparing these results to the dispersion relations calculated by Maeda *et al.*[24] for pristine graphite we can trace the origin of almost all the phonon branches of the intercalation compounds to the corresponding phonon branches in graphite. For stages $n \geq 3$, we observe that for frequencies greater than 800 cm^{-1} there are two phonon branches that track each other. This is more apparent in Fig. 5 where the phonon dispersion relations for a stage-3 acceptor compound are plotted for various high-symmetry directions throughout the zone. These tracking branches are identified on the basis of their eigenvectors to be a mode splitting into graphite bounding and interior layer modes. This is one of the important conclusions of our calculation, and confirms the interpretation that had previously been given for the observed Raman spectra.[3,10] The calculations further show a very small splitting of each of the interior layer modes (by ~ 0.5 cm^{-1}) depending on the distance of the interior layer to the nearest graphite bounding layer, so that for a stage-n compound ($n \geq 3$), there would be approximately $(n-2)/2$ nearly degenerate graphite interior layer modes. These nearly degenerate modes are not resolved in the Raman spectra, but this near degeneracy explains why the linewidth of the graphite interior layer ($E^0_{2g_2}$) mode tends to be greater than that for the graphite bounding layer ($\hat{E}_{2g_2}$).

The $C_{2n}X$ model does not, however, account for the sign of the shift of the high-frequency infrared-active bounding layer mode near 1600 cm^{-1}. This result is not surprising for the following reasons. Firstly, in pristine graphite, the dynamical matrix in the Born–von Kármán formalism fails to account for the magnitude and sign of the Davydov splitting of the E_{1u} infrared-active mode and the E_{2g_2} Raman-active mode. Expansion to fourth neighbor out-of-plane interactions is necessary to obtain the terms which determine the

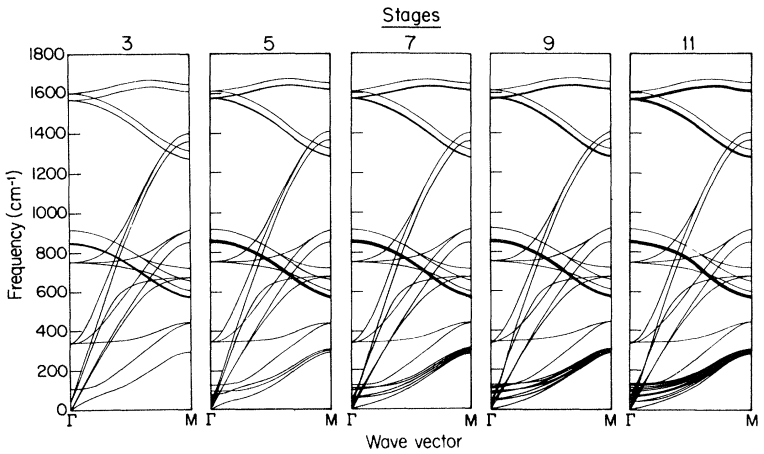

FIG. 4. Phonon dispersion curves calculated for stages 3, 5, 7, 9, and 11 donor compounds using the $C_{2n}X$ model and the parameters given in Tables I and V. The dispersion curves for the acceptor compounds show only small shifts to higher frequencies.

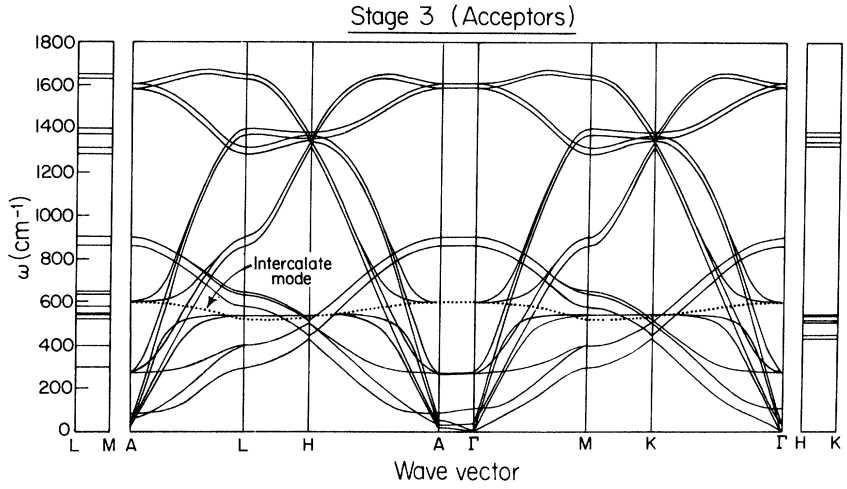

FIG. 5. Phonon dispersion relations calculated for a $C_{2n}X$ acceptor compound for stage 3 ($n=3$) along several high-symmetry axes. Note that most of the graphitic branches occur in pairs and the corresponding normal modes show that each member of the pair is associated with either a graphite bounding layer or a graphite interior layer. The frequencies of the branch labeled "intercalate mode" are very sensitive to the choice of the intercalate-related parameters given in Table V. There are other intercalatelike modes in the 100-cm^{-1} region.

Davydov splitting and also satisfy the elastic constants for pristine graphite.[47] Secondly, the in-plane infrared-active mode involves displacements in two graphite layers, whereas the in-plane Raman-active mode requires only a single graphite layer.

The $C_{2n}X$ model, moreover, predicts a significant dependence of the A_{2u} infrared-active mode on intercalation. Preliminary experimental results for the behavior of the A_{2u} mode in graphite-$FeCl_3$ acceptor compounds show qualitative agreement with the predictions of the $C_{2n}X$ model.[48]

The advantage of a symmetry derived phenomenological model can be seen in Fig. 4. Once the problem is set up and the parameters are obtained for a certain stage and intercalant, one can easily calculate the dispersion relations for an arbitrary stage with *no* additional parameters. The physical basis for this approach is that different stage compounds of a given intercalant consists of two very similar building blocks: (1) an intercalate layer sandwiched between two graphite bounding layers, and (2) $n-2$ graphite interior layers. Explicit extensions to other superlattices can be easily implemented or can be inferred from in-plane zone folding of the appropriate high-symmetry points in the $C_{2n}X$ structure. The model indicates that the phonon dispersion relations for the high-stage compounds ($n \geq 3$) are similar to each other, except for the near degeneracy of some of the phonon branches. The model further points out that the low-frequency branches are split increasingly as the stage index increases, suggesting that experiments such as inelastic neutron scattering which are sensitive to these branches will provide important data for evaluating the parameters of the model for specific intercalants.

The model for the $C_{2n}X$ structure also gives branches identified with the intercalant and such branches are shown in Fig. 5 and labeled "intercalate mode." This identification is made by considering the atomic vibrations (eigenfunctions) at the zone center, which for these modes are shown to involve atomic motions in the intercalate layer. It is to be noted that in the $C_{2n}X$ model, we have overestimated the in-plane density of intercalate atoms commonly occurring in graphite intercalation compounds. The $C_{2n}X$ model, thus, includes too many intercalant-intercalant interactions, thereby leading to an overestimate of the intercalate frequencies.

On the other hand, the $C_{2n}X$ model treats the intercalate layer more successfully than the modified graphite layer model, which yields the unphysical result of an intercalant mode above 1600 cm^{-1}. This unphysical mode can be considered within the context of the shell model for phonons as a low-lying electronic excitation which interacts strongly with the lattice modes.

To further explore the implications of our model, the dispersion along the ΓA axis for the low-frequency branches has been calculated for stages $3 \leq n \leq 11$ and the results are shown in Fig. 6 on an expanded scale. Our calculations show that these branches are relatively independent of

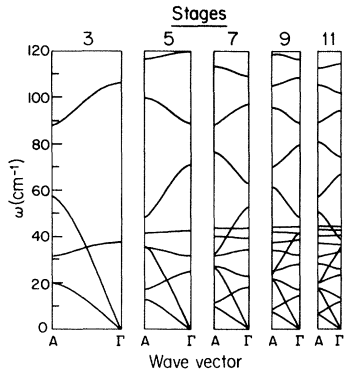

FIG. 6. Phonon dispersion curves along the ΓA axis for the low-frequency branches for graphite intercalation compounds with stages 3, 5, 7, 9, and 11, calculated using the $C_{2n}X$ model. The parameters for the calculation are given in Tables I and V. The results for the donor and acceptor compounds are almost identical along this axis and are not illustrated separately.

whether the compound is a donor or an acceptor compound and depend mainly on the stage. This observation can be explained by the following arguments: (1) The dominant effect in the dispersion curves along ΓA is associated with k_z-axis zone folding. (2) The distinction between a donor and an acceptor compound within this model is the sign of the stage dependence of the in-plane force constants; these force constants have little effect on the dispersion relations along ΓA; and (3) the intercalant-graphite bounding layer interactions affect most strongly the acoustic branches, and branches having the same symmetries. The strong short-range bonding of the intercalant to the graphite bounding layer for both donors and acceptors implies that the effect of intercalation on the interlayer force constants should be similar. Because of the increased bonding between the graphite bounding layer and the intercalant, the bonding to the adjacent graphite layer is weakened for stages $n \geq 2$.

It is anticipated that the results for the low-frequency branches shown in Fig. 6 will require modification as further experimental information on the low-frequency phonon spectra of graphite intercalation compounds become available. It is in these low-frequency branches that the dominant stage dependence is found, both in the number of phonon branches and the value of the mode frequencies, including the zone-center mode frequencies that can be observed by Raman and infrared spectroscopy. Figure 6 shows that the low-frequency modes depart significantly from a simple zone folding of the graphite dispersion relations and that replacing a graphite layer by an intercalate layer is important in determining the dispersion relations in these compounds. From the initial slope of the acoustic branches, we can calculate the transverse and longitudinal sound velocities for propagation along the c axis. The resulting longitudinal and transverse sound velocities and the elastic constants C_{33} and C_{44} are listed in Table VI for several stages for our model intercalant. Based on this model and the values selected for the parameters, both the velocity of sound and the

TABLE VI. Calculated velocities of sound and elastic constants.

Stage	ρ (g/cm^3)[a]	v_z^t (10^5 cm/s)	C_{44} (10^{10} g/cm s)	v_z^l (10^5 cm/s)	C_{33} (10^{11} g/cm s)
1[b]	1.751	19.413	654.00	19.524	65.400
3	2.001	2.137	9.138	5.970	7.130
5	2.096	1.820	6.941	5.110	5.473
7	2.144	1.687	6.102	4.772	4.882
9	2.172	1.627	5.750	4.600	4.596
11	2.191	1.591	5.542	4.507	4.452
HOPG[c]	2.286	1.414	4.572	4.017	3.690
			4.2[d]		3.90[d]

[a]In calculating the density ρ, we have taken equal values for the intercalant and carbon masses per unit area and $I_c=(n+\frac{1}{2})c_0$.

[b]The stage-1 values for the velocity of sound and the elastic constants are obtained using the same force-constant parameters as for the stage-3 compound. The values obtained for the velocities of sound and elastic constants are too high to be physically meaningful, indicating that the nature of the coupling is different for the stage-1 compound, where the graphite layer is bounded on *both* sides by an intercalant layer.

[c]HOPG denotes highly oriented pyrolytic graphite, a form of pristine graphite (Ref. 49).

[d]Experimental values from neutron scattering data (Ref. 31).

elastic constants along the c axis show an increase relative to the corresponding values for graphite. The stiffening of the acoustic branches implies that the Debye temperature should increase upon intercalation, in agreement with specific-heat results for graphite-Li,[21] but not with those for the heavy alkali-metal compounds.[20,23] It is further observed that the values for the stage-1 compound are anomalously high. This is because the interaction between the graphite and intercalate layers is different for stage 1 since the graphite bounding layer is sandwiched between two intercalate layers, thereby requiring a modification of the interaction parameters.

Using the calculated phonon dispersion relations, we have plotted the phonon density of states for a number of compounds[46] and the results are shown in Fig. 7 for stage-1 and -3 donor and acceptor compounds. The phonon density of states curve shows that the strongest single feature is the mode at ~ 600 cm^{-1} that comes from the high density of states at and near the Brillouin-zone edges. This high density of states near 600 cm^{-1} is more pronounced in intercalated graphite than in pure graphite, and the magnitude of this peak decreases with increasing stage. Other features in the density of states curves for the intercalation compounds can be identified with features in the density of states in pristine graphite, with roughly the same relative contributions from the various modes. From the density of states results, we can calculate the second-order Raman spectra and the specific heat.

V. CONCLUSIONS

We have presented the first general calculation of the phonon dispersion relations of a stage-n graphite intercalation compound. In our calculation the symmetry of the staging phenomenon is exploited by using the k_z-axis zone-folding technique. The calculation is performed on generalized donor and acceptor compounds without specific reference to the intercalant species. Three limiting cases are considered: (a) the empty intercalate layer limit where the intercalate layer is approximated by vacuum, (b) the modified graphite layer limit where the intercalate layer is a graphite layer with a modified in-plane mass density, and (c) the $C_{2n}X$ structure with a modified site occupation in the intercalate layer. For the empty intercalate layer limit, the phonon dispersion relations are essentially the same as those for zone-folded pristine

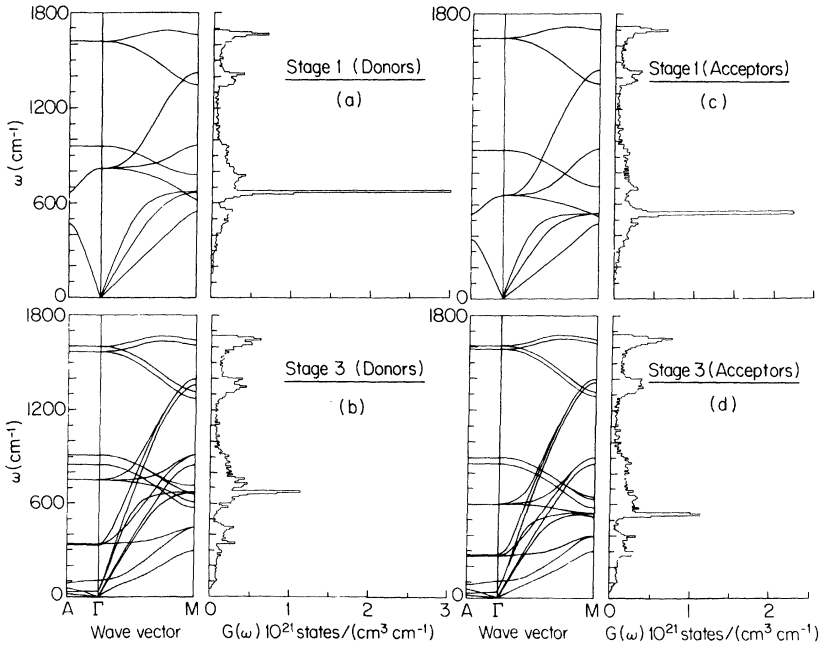

FIG. 7. Phonon dispersion curves and density of states $G(\omega)$ for stage-1 and -3 acceptor and donor compounds using the $C_{2n}X$ model. The parameters used in this calculation are given in Tables I and V. Note the overall similarities in the density of states for donor and acceptor compounds of the same stage, except that the peak in $G(\omega)$ near ~ 570 cm^{-1} is most intense for the stage-1 donor compound (a), somewhat less intense for the stage-1 acceptor (c), and of still lesser intensity for the stage-3 donor (b) and acceptor (d) compounds.

graphite except that there are six fewer modes and there is, in addition, a loss of k_z-axis dispersion. The modified graphite layer limit is simple to implement and is able to explain the experimentally observed splitting between the graphite bounding and interior layer Raman-active modes. The model predicts very large shifts of the A_{2u} infrared-active out-of-plane graphite mode which are of interest to study experimentally. However, the modified graphite layer model has the unphysical feature of yielding an intercalant mode at frequencies much higher than 1600 cm^{-1}. The possible interpretation of this high-frequency mode as a shell or internal mode makes this model attractive for modeling acceptor compounds which are known to have internal modes and which generally are also structurally incommensurate with the graphite.

The $C_{2n}X$ structure is found to be the most physical of the three limiting cases for modeling donor compounds. In the $C_{2n}X$ structure the metal ion lies over the center of the carbon hexagon, and the resulting model gives agreement with experimental results for the magnitude and frequency shift of the high-frequency Raman-active mode (~ 1600 cm^{-1}) resulting from intercalation. For the particular parameters that were chosen, the transverse intercalate mode is identified as one of the modes near ~ 600 cm^{-1}.

The $C_{2n}X$ model is also able to account for the observation of very few high-frequency optic modes in the intercalation compounds. The model shows that most of the highly perturbed graphite modes are below 400 cm^{-1}. These low-frequency modes are more difficult to study with both Raman and infrared spectroscopy than the modes above ~ 400 cm^{-1}. Second-order Raman spectra, far infrared measurements, and inelastic neutron scattering experiments will be especially important for providing further experimental data for determining the parameters of the model for specific compounds.

The folded $C_{2n}X$ model does not, however, account for the sign of the shift of the high-frequency infrared-active bounding layer mode around 1600 cm^{-1}. This result is not surprising for the following reasons: (1) In pristine graphite the Maeda model for the dynamical matrix in the Born—von Kármán formalism fails to account for the magnitude and sign of the Davydov splitting of the E_{1u} infrared-active mode and the E_{2g_2} Raman-active mode. Expansion to second interplane neighbors[47] is needed to obtain the Davydov splitting correctly. (2) The in-plane infrared-active mode involves displacements in two graphite layers, while the in-plane Raman-active mode needs only one graphite layer. Thus the infrared-active modes would be expected to be more sensitive to the detailed in-plane superlattice structure of the intercalant. Finally, (3) in-plane zone folding is not considered in this model. The inclusion of in-plane zone folding results in new zone-center modes some of which are optically active.

Further work suggested for the modeling of the lattice dynamics of the intercalation compounds includes: (1) explanation of the observed splitting of the infrared-active modes, (2) detailed fitting of the Raman and infrared-active modes by including the interactions with further neighbors, (3) incorporation of in-plane zone folding, (4) more quantitative determination of the interaction parameters as more experimental results become available, and (5) detailed fitting to specific compounds by explicitly including the intercalant-intercalant parameters. Since the completion of the present work, further neutron scattering experiments[54] have provided more detailed experimental data on the low-frequency c-axis modes. Modification of the present calculation to fit these new data is in preparation.[55]

Note added in proof: Since the completion of the present work, further neutron scattering experiments[54] have provided more detailed experimental data on the low-frequency c-axis modes. Modification of the present calculation to fit these new data is in preparation.[55]

ACKNOWLEDGMENTS

We gratefully acknowledge support from ONR Grant No. N00014-77-0053 for this work. The Francis Bitter National Magnet Laboratory is supported by NSF.

APPENDIX A: DYNAMICAL MATRIX FOR HEXAGONAL GRAPHITE

The site locations for the four distinct carbon atoms A, A', B, and B' per unit cell shown in Fig. 1 are given by

$$\begin{aligned} \vec{\tau}_A &= 0 , \\ \vec{\tau}_B &= (\vec{a}_1 - \vec{a}_2)/3 , \\ \vec{\tau}_{A'} &= \vec{a}_3/2 , \\ \vec{\tau}_{B'} &= (2\vec{a}_1 + \vec{a}_2)/3 + \vec{a}_3/2 , \end{aligned} \tag{A1}$$

where the hexagonal basis vectors are

$$\vec{a}_1 = a_0\hat{y}\ ,$$
$$\vec{a}_2 = -a_0(\hat{x}\sqrt{3}+\hat{y})/2\ , \tag{A2}$$
$$\vec{a}_3 = c_0\hat{z}\ ,$$

and $\hat{x}$, $\hat{y}$, $\hat{z}$ are unit vectors along the orthogonal axes, and $a_0 = 2.46$ Å and $c_0 = 3.35$ Å are the lattice constants. The wave vectors in reciprocal lattice space are given by

$$\vec{K}_1 = 2\pi(-\hat{x}+\hat{y}\sqrt{3})/(\sqrt{3}a_0)\ ,$$
$$\vec{K}_2 = -4\pi\hat{x}/(\sqrt{3}a_0)\ , \tag{A3}$$
$$\vec{K}_3 = 2\pi\hat{z}/c_0\ .$$

The general lattice sites in the real lattice are given by

$$\vec{r}(l\kappa) = l_1^0\vec{a}_1 + l_2^0\vec{a}_2 + l_3^0\vec{a}_3 + \vec{\tau}_\kappa \tag{A4}$$

in which $l\kappa$ denotes the κth atom in the lth unit cell and $l_1^0 = l_1/3$, $l_2^0 = l_2/3$, and $l_3^0 = l_3/2$.

The dynamical matrix for lattice vibrations is defined by Eq. (1) and values for the force constants for graphite are given in Table I. If one takes the axis $x'(l\kappa;l'\kappa')$ to coincide with $\vec{r}(l\kappa)-\vec{r}(l'\kappa')$ in defining the in-plane force constants, and takes the force constants with only the tangential and radial components $(\phi_{ti}^{(n)}, \phi_{to}^{(n)}, \phi_r^{(n)})$, then the force-constant matrix is given by

$$\tilde{\Phi}(l\kappa;l'\kappa') = \begin{bmatrix} \phi_r^{(n)} & 0 & 0 \\ 0 & \phi_{ti}^{(n)} & 0 \\ 0 & 0 & \phi_{to}^{(n)} \end{bmatrix}, \tag{A5}$$

where n denotes the nth in-plane neighbor and is determined by $\vec{r}(l\kappa)-\vec{r}(l'\kappa')$.

For the out-of-plane force constants, we let the $z'(l\kappa;l'\kappa')$ axis coincide with $\vec{r}(l\kappa)-\vec{r}(l'\kappa')$, and taking only the tangential and radial components $(\hat{\phi}_t^{(n)}, \hat{\phi}_r^{(n)})$, we have

$$\tilde{\Phi}(l\kappa;l'\kappa') = \begin{bmatrix} \hat{\phi}_t^{(n)} & 0 & 0 \\ 0 & \hat{\phi}_t^{(n)} & 0 \\ 0 & 0 & \hat{\phi}_r^{(n)} \end{bmatrix}. \tag{A6}$$

The force-constant matrix in the (x',y',z') coordinate system $\tilde{\Phi}(l\kappa;l'\kappa')$ is related to the force-constant matrix in the (x,y,z) coordinate system $\tilde{\phi}(l\kappa;l'\kappa')$ by

$$\tilde{\Phi}(l\kappa;l'\kappa') = R^{-1}\tilde{\phi}(l\kappa;l'\kappa')R\ , \tag{A7}$$

where R is the appropriate rotational matrix:

$$R(\theta,\zeta) = \begin{bmatrix} \cos\theta\cos\zeta & \sin\theta\cos\zeta & -\sin\zeta \\ -\sin\theta & \cos\theta & 0 \\ \cos\theta\sin\zeta & \sin\theta\sin\zeta & \cos\zeta \end{bmatrix}. \tag{A8}$$

For in-plane neighbors $\zeta = 0$, and thus the in-plane force-constant matrix takes the form

$$\tilde{\Phi}(l\kappa;l'\kappa') = \begin{bmatrix} \phi_r^{(n)}\cos^2\theta + \phi_{ti}^{(n)}\sin^2\theta & (\phi_r^{(n)}-\phi_{ti}^{(n)})\sin\theta\cos\theta & 0 \\ (\phi_r^{(n)}-\phi_{ti}^{(n)})\sin\theta\cos\theta & \phi_r^{(n)}\sin^2\theta + \phi_{ti}^{(n)}\cos^2\theta & 0 \\ 0 & 0 & \phi_{to}^{(n)} \end{bmatrix}. \tag{A9}$$

The out-of-plane force-constant matrix given by Eqs. (A6) and (A7) using the appropriate values for θ and ζ which are given in Ref. 46 for up to third-neighbor in-plane and second-neighbor out-of-plane interactions. The terms $\phi_{\alpha\beta}(l\kappa;l'\kappa')$ appearing in Eq. (1) are the $\alpha\beta$ components of the matrix $\tilde{\phi}(l\kappa;l'\kappa')$. The dynamical matrix can be expressed in the symmetrized form which is discussed in Appendix B.

APPENDIX B: MATRIX ELEMENTS OF THE DYNAMICAL MATRIX FOR PRISTINE GRAPHITE

The dynamical matrix of Eq. (1) is expressed as an expansion in l and l', which relates to the various possible distances between carbon atoms $\vec{r}(l\kappa)-\vec{r}(l'\kappa')$. The dependence of the expansion on wave vector $\vec{k}$ is given by the exponential plane waves, which are more conveniently written in a symmetrized form in terms of the Fourier functions $F^{\Gamma_i}(\vec{l},\vec{\xi})$, listed in Table II in order of increasing carbon-carbon (C-C) atom separations, starting with the constant term $\vec{l}=000$, the nearest-neighbor term 100, and more distant neighbor terms 210, etc. The coefficients $a_{\alpha\beta}^{\Gamma_i}(\vec{l},\nu)$ are the Fourier expansion parameters, which are related in Table III to the force constants that have previously been determined for graphite by Maeda *et al.*[24]

The symmetry relations given by Eqs. (6) and (7), establish all terms in the dynamical matrix. Given below are all the matrix elements of Eq. (5) determined for the graphite symmetry. In the case

of the $F^{\Gamma_i}(000,\vec{\xi})$ terms, the Fourier parameters assume different values depending on whether the $a^{\Gamma_i}_{\alpha\beta}(\vec{l},\nu)$ parameters are indexed by an A, A', B, or B' subscript for the site designation.

The dynamical matrix for pristine graphite can be written in a form which is identical mathematically to the Fourier expansion[50–52] for the electronic p bands (both π and σ bands) in graphite.[53] The dynamical matrix is Hermitian and takes the form

$$D_g^{sym}=\begin{bmatrix} D_{aa}(\vec{k}) & D_{ab}(\vec{k}) \\ D_{ab}^{\dagger}(\vec{k}) & D_{bb}(\vec{k}) \end{bmatrix} \tag{B1}$$

in which the 6×6 blocks $D_{\alpha\beta}(\vec{k})$ are given by

$$D_{\alpha\beta}(\vec{k})=\begin{bmatrix} D_{\alpha\beta}^{A_{1g}}(\vec{k}) & D_{\alpha\beta}^{B_{2u}}(\vec{k}) \\ D_{\alpha\beta}^{B_{2u}}(\vec{k}+\vec{K}_3) & D_{\alpha\beta}^{A_{1g}}(\vec{k}+\vec{K}_3) \end{bmatrix} \tag{B2}$$

and symmetry requires

$$D_{\alpha\alpha}^{B_{2u}}(\vec{k}+\vec{K}_3)=D_{\alpha\alpha}^{B_{2u}}(\vec{k})^{\dagger}\ , \tag{B3a}$$

while for the aa and bb diagonal blocks in Eq. (B1), symmetry requires

$$D_{aa}(\vec{k}\pm\vec{K}_2)=D_{aa}(\vec{k})\ , \tag{B3b}$$

$$D_{bb}^{\Gamma_i}(\vec{k}\pm\vec{K}_2)=\{D_{bb}^{\Gamma_i}(\vec{k})+3D_{bb}^{\Gamma_i}(\vec{k}+\vec{K}_3)\pm i\sqrt{3}[D_{bb}^{\Gamma_j}(\vec{k})-D_{bb}^{\Gamma_j}(\vec{k}+\vec{K}_3)]\}/4\ , \tag{B3c}$$

in which Γ_j denotes the direct product representation $\Gamma_j=\Gamma_i\times B_{2u}$. For the off-diagonal blocks ($\alpha\neq\beta$) in Eq. (B1), symmetry requires

$$D_{\alpha\beta}^{\Gamma_i}(\vec{k}\pm\vec{K}_2)=-[D_{\alpha\beta}^{\Gamma_i}(\vec{k})\pm i\sqrt{3}D_{\alpha\beta}^{\Gamma_j}(\vec{k})]/2\ , \tag{B3d}$$

where $\vec{K}_2$ and $\vec{K}_3$ are defined in Eq. (A3) and the 3×3 blocks with symmetry $\Gamma_i=A_{1g}$ or B_{2u} are written in terms of the dimensionless wave vector $\vec{\xi}$ as

$$D_{\alpha\beta}^{\Gamma_i}(\vec{\xi})=\sum_l\sum_\nu a_{\alpha\beta}^{\Gamma_i}(\vec{l},\nu)\{F^{\Gamma_j}(\vec{l},\vec{\xi});\sigma_\nu(\Gamma_k)\}_{\Gamma_i}\ , \tag{B4}$$

where linear combinations of the products $F^{\Gamma_j}(\vec{l},\vec{\xi})\sigma_\nu(\Gamma_k)$ are taken to obtain that component which transforms as Γ_i. The nine basis matrixes $\sigma_\nu(\Gamma_k)$ used in the Fourier expansion of Eq. (B4) are given by[50]

$$\sigma_1(A_{1g})=S_{\sigma\sigma}^{e}(A_{1g})=\begin{bmatrix}1&0&0\\0&1&0\\0&0&0\end{bmatrix}\ , \tag{B5a}$$

$$\sigma_2(A_{2g})=S_{\sigma\sigma}^{o}(A_{2g})=\begin{bmatrix}1&0&0\\0&-1&0\\0&0&0\end{bmatrix}\ , \tag{B5b}$$

$$\sigma_3(E_{2g})=S_{\sigma\sigma}^{e}(E_{2g})=\begin{bmatrix}0&1&0\\0&0&0\\0&0&0\end{bmatrix}\ ,\ \begin{bmatrix}0&0&0\\1&0&0\\0&0&0\end{bmatrix}\ , \tag{B5c}$$

$$\sigma_4(A_{1g})=S_{\pi\pi}^{e}(A_{1g})=\begin{bmatrix}0&0&0\\0&0&0\\0&0&1\end{bmatrix}\ , \tag{B5d}$$

$$\sigma_5(E_{1g})=S_{\pi\sigma}^{e}(E_{1g})=\begin{bmatrix}0&0&0\\0&0&-i\\-i&0&0\end{bmatrix}\ ,\ \begin{bmatrix}0&0&i\\0&0&0\\0&i&0\end{bmatrix}\ , \tag{B5e}$$

$$\sigma_6(E_{1g})=S_{\pi\sigma}^{o}(E_{1g})=\begin{bmatrix}0&0&0\\0&0&1\\-1&0&0\end{bmatrix}\ ,\ \begin{bmatrix}0&0&-1\\0&0&0\\0&1&0\end{bmatrix}\ , \tag{B5f}$$

in which e and o represent the even and odd symmetry under time inversion. The dynamical matrix must be even under time inversion; hence the diagonal blocks $D_{aa}(\vec{k})$ and $D_{bb}(\vec{k})$ are expanded using the spin matrices which are even under time inversion whereas the off-diagonal block $D_{ab}(\vec{k})$ can have both even and odd terms. The constraint on the dynamical matrix, Eq. (B1), imposed by the requirement that there be no restoring force for a uniform displacement is that at $\vec{\xi}=0$ the acoustic mode and all couplings to the acoustic mode vanish identically.

The dynamical matrix in the site representation in Eq. (5) is obtained from the symmetrized form of the dynamical matrix derived in this appendix by the unitary transformation

$$D_g(\vec{k})=VD_g^{\rm sym}(\vec{k})V^{-1} \tag{B6}$$

in which

$$V=\frac{1}{\sqrt{2}}\begin{bmatrix}1&1&0&0\\0&0&1&1\\1&-1&0&0\\0&0&1&-1\end{bmatrix} \tag{B7}$$

and 0 and 1 are 3×3 null and unit matrices, respectively.

In the transformed site representation the dynamical matrix for pristine graphite is given by Eq. (5) where the matrix elements are given by

$$D_{\alpha\beta}(\vec{\xi})=\begin{bmatrix}\delta_{11}^{\alpha\beta}(\vec{\xi})&\delta_{12}^{\alpha\beta}(\vec{\xi})&\delta_{13}^{\alpha\beta}(\vec{\xi})\\ \delta_{12}^{\alpha\beta^*}(\vec{\xi})&\delta_{22}^{\alpha\beta}(\vec{\xi})&\delta_{13}^{\alpha\beta^*}(\vec{\xi})\\ \delta_{13}^{\alpha\beta^*}(\vec{\xi})&\delta_{13}^{\alpha\beta}(\vec{\xi})&\delta_{33}^{\alpha\beta}(\vec{\xi})\end{bmatrix}, \tag{B8}$$

where $\alpha,\beta=A$, B, A', and B', and the basis vectors are $(x+iy, x-iy, z)$. For $\alpha\beta=AA$, AA', $A'A'$, BB, and $B'B'$, we have

$$\delta_{11}^{\alpha\beta}(\vec{\xi})=\sum_l a_{\alpha\beta}^{A_{1g}}(\vec{l},1)F^{A_{1g}}(\vec{l},\vec{\xi})+\sum_l a_{\alpha\beta}^{B_{2u}}(\vec{l},2)F^{B_{1u}}(\vec{l},\vec{\xi}), \tag{B9a}$$

$$\delta_{22}^{\alpha\beta}(\vec{\xi})=\sum_l a_{\alpha\beta}^{A_{1g}}(\vec{l},1)F^{A_{1g}}(\vec{l},\vec{\xi})-\sum_l a_{\alpha\beta}^{B_{2u}}(\vec{l},2)F^{B_{1u}}(\vec{l},\vec{\xi}), \tag{B9b}$$

$$\delta_{33}^{\alpha\beta}(\vec{\xi})=\sum_l a_{\alpha\beta}^{A_{1g}}(\vec{l},4)F^{A_{1g}}(\vec{l},\vec{\xi}), \tag{B9c}$$

$$\delta_{12}^{\alpha\beta}(\vec{\xi})=\sum_l a_{\alpha\beta}^{A_{1g}}(\vec{l},3)F^{E_{2g}}(\vec{l},\vec{\xi}), \tag{B9d}$$

$$\delta_{13}^{\alpha\beta}(\vec{\xi})=i\sum_l a_{\alpha\beta}^{A_{1g}}(\vec{l},5)F^{E_{1g}^*}(\vec{l},\vec{\xi})+\sum_l a_{\alpha\beta}^{B_{2u}}(\vec{l},6)F^{E_{2u}^*}(\vec{l},\vec{\xi}), \tag{B9e}$$

and for $\alpha\beta=BB'$,

$$\delta_{11}^{\alpha\beta}(\vec{\xi})=\sum_l a_{\alpha\beta}^{A_{1g}}(\vec{l},1)[F^{A_{1g}}(\vec{l},\vec{\xi})+F^{B_{2u}}(\vec{l},\vec{\xi})], \tag{B10a}$$

$$\delta_{22}^{\alpha\beta}(\vec{\xi})=\delta_{11}^{\alpha\beta}(\vec{\xi}), \tag{B10b}$$

$$\delta_{33}^{\alpha\beta}(\vec{\xi})=\sum_l a_{\alpha\beta}^{A_{1g}}(\vec{l},4)[F^{A_{1g}}(\vec{l},\vec{\xi})+F^{B_{2u}}(\vec{l},\vec{\xi})], \tag{B10c}$$

$$\delta_{12}^{\alpha\beta}(\vec{\xi})=\sum_l a_{\alpha\beta}^{A_{1g}}(\vec{l},3)[F^{E_{2g}}(\vec{l},\vec{\xi})+F^{E_{1u}}(\vec{l},\vec{\xi})], \tag{B10d}$$

$$\delta_{13}^{\alpha\beta}(\vec{\xi})=i\sum_l a_{\alpha\beta}^{A_{1g}}(\vec{l},5)[F^{E_{1g}^*}(\vec{l},\vec{\xi})-F^{E_{2u}^*}(\vec{l},\vec{\xi})], \tag{B10e}$$

and for $\alpha\beta=AB$ and $A'B$,

$$\delta_{11}^{\alpha\beta}(\vec{\xi})=\sum_l a_{\alpha\beta}^{A_{1g}}(\vec{l},1)[F^{A_{1g}}(\vec{l},\vec{\xi})+F^{B_{2u}}(\vec{l},\vec{\xi})]+i\sum_l a_{\alpha\beta}^{B_{2u}}(\vec{l},2)[F^{A_{2g}}(\vec{l},\vec{\xi})+F^{B_{1u}}(\vec{l},\vec{\xi})], \tag{B11a}$$

$$\delta_{22}^{\alpha\beta}(\vec{\xi})=\sum_l a_{\alpha\beta}^{A_{1g}}(\vec{l},1)[F^{A_{1g}}(\vec{l},\vec{\xi})+F^{B_{2u}}(\vec{l},\vec{\xi})]-i\sum_l a_{\alpha\beta}^{B_{2u}}(\vec{l},2)[F^{A_{2g}}(\vec{l},\vec{\xi})+F^{B_{1u}}(\vec{l},\vec{\xi})], \tag{B11b}$$

$$\delta_{33}^{\alpha\beta}(\vec{\xi})=\sum_l a_{\alpha\beta}^{A_{1g}}(\vec{l},4)[F^{A_{1g}}(\vec{l},\vec{\xi})+F^{B_{2u}}(\vec{l},\vec{\xi})], \tag{B11c}$$

$$\delta_{12}^{\alpha\beta}(\vec{\xi})=\sum_l a_{\alpha\beta}^{A_{1g}}(\vec{l},3)[F^{E_{2g}}(\vec{l},\vec{\xi})+F^{E_{1u}}(\vec{l},\vec{\xi})], \tag{B11d}$$

$$\delta_{13}^{\alpha\beta}(\vec{\xi})=i\sum_l a_{\alpha\beta}^{A_{1g}}(\vec{l},5)[F^{E_{1g}^*}(\vec{l},\vec{\xi})-F^{E_{2u}^*}(\vec{l},\vec{\xi})]+i\sum_l a_{\alpha\beta}^{B_{2u}}(\vec{l},6)\times[F^{E_{1g}^*}(\vec{l},\vec{\xi})-F^{E_{2u}^*}(\vec{l},\vec{\xi})]. \tag{B11e}$$

In the above equations $F^{\Gamma_i^*}(\vec{l},\vec{\xi})$ denotes the complex conjugate of the function $F^{\Gamma_i}(\vec{l},\vec{\xi})$. In the sums over l which occur in the above equations (B9), (B10), and (B11), the nonzero values for $a^{\Gamma_i}_{\alpha\beta}(l,\nu)$ are obtained from the $\vec{k}$-space translational properties [see Eq. (B3)] and are given explicitly in the site representation as

$$\begin{aligned}
&\text{for } \alpha\beta=AA\text{: } l_1,l_2=0, \text{ mod } 3;\ l_3=0, \text{ mod } 2\ ,\\
&\text{for } \alpha\beta=BB\text{: } l_1,l_2=0, \text{ mod } 3;\ l_3=0, \text{ mod } 2\ ,\\
&\text{for } \alpha\beta=AB\text{: } l_1,l_2\neq 0, \text{ mod } 3;\ l_3=0, \text{ mod } 2\ ,\\
&\text{for } \alpha\beta=AA'\text{: } l_1,l_2=0, \text{ mod } 3;\ l_3=1, \text{ mod } 2\ ,\\
&\text{for } \alpha\beta=AB'\text{: } l_1,l_2\neq 0, \text{ mod } 3;\ l_3=1, \text{ mod } 2\ ,\\
&\text{for } \alpha\beta=BB'\text{: } l_1,l_2\neq 0, \text{ mod } 3;\ l_3=1, \text{ mod } 2\ ,
\end{aligned} \tag{B12}$$

and for $l_1,l_2\neq 0$, mod 3, we impose the further constraint $l_1\neq l_2$.

APPENDIX C: UNITARY TRANSFORMATION FROM THE ZONE-FOLDED REPRESENTATION TO THE LAYER REPRESENTATION

The dynamical matrix is written in the site representation where the lattice displacement $u_\alpha(l\kappa)$ takes the form

$$u_\alpha(l\kappa)=(M_\kappa)^{-1/2}U_\alpha(\kappa)\exp[-i\omega t+i\vec{k}\cdot\vec{r}(l\kappa)]\ , \tag{C1}$$

in which M_κ and $U_\alpha(\kappa)$ are the mass and normal-mode coordinate for atom κ. One can then write

$$U_\alpha(\kappa)=(M_\kappa)^{-1/2}\sum_l u_\alpha(l\kappa)\exp[i\omega t-i\vec{k}\cdot\vec{r}(l\kappa)]\ , \tag{C2}$$

where $\vec{r}(l\kappa)=\vec{r}(l)+\tau(\kappa)$, $\vec{r}(l)$ is a lattice vector of the Bravais lattice, and $\vec{\tau}(\kappa)$ labels the equivalent sites within the unit cell. The derivation of the unitary transformation to a layer representation follows the same steps as given in Ref. 1 for the unitary transformation for the electronic energy bands. The resulting unitary matrix is given by

$$U=1/\sqrt{l}\begin{vmatrix} \Omega_{00} & \cdots & \Omega_{l-1,0} \\ \vdots & & \vdots \\ \Omega_{0,l-1} & \cdots & \Omega_{l-1,(l-1)^2} \end{vmatrix}\ , \tag{C3}$$

where $\Omega_{p,m}$ is a 12×12 diagonal matrix of the form

$$\Omega_{p,m}=\exp\left[\frac{2\pi i m}{l}\right]\begin{vmatrix} \underline{1} & \underline{0} \\ \underline{0} & \gamma_p\underline{1} \end{vmatrix}\ , \tag{C4}$$

where

$$\gamma_p=\exp\left[\frac{2\pi i p}{l}\right]$$

and $\underline{1}$ and $\underline{0}$ are 6×6 unit and null matrices.

APPENDIX D: INTERCALATE TERMS IN THE DYNAMICAL MATRIX

The case for a perfectly ordered commensurate intercalate in-plane superlattice can be treated exactly within the Born–von Kármán treatment of lattice dynamics. This appendix formulates this model mathematically.

We consider a single layer, intercalated with one atom per unit superlattice cell. This introduces a 3×3 intercalate block D_{XX} in the dynamical matrix which we can write as a Fourier expansion in the layer representation as

$$D^{A_{1g}}_{XX}(\vec{\xi})=\sum_{\Gamma_j}\sum_l a^{A_{1g}}_{XX}(\vec{l},\nu)\{F^{\Gamma_j}(\vec{l},\vec{\xi});\sigma_\nu(\Gamma_k)\}_{A_{1g}} \tag{D1}$$

in which the basis matrices $\sigma_\nu(\Gamma_k)$ are as defined in Eqs. (B5). The expansion in Eq. (D1) is identical to that given in Eqs. (B4) of Appendix B with the replacement of $\alpha\beta$ by XX. The sum over l in Eq. (D1) for a $(\sqrt{l_s}\times\sqrt{l_s})$ in-plane superlattice will depend on l_s. Explicitly the sum will be over all l for a $p(1\times 1)$ superlattice (i.e., the $C_{2n}X$ model), or over every other l for a $p(2\times 2)$ superlattice (i.e., the $C_{8n}X$ model). The sum over l_3 for the out-of-plane superlattice contains terms every $n+1$ integers for a stage n compound.

One can similarly expand the graphite-intercalate interaction terms in a Fourier expansion as

$$D^{\Gamma_i}_{XG}(\vec{k})=\sum_\nu\sum_l a^{\Gamma_i}_{XG}(\vec{l},\nu)\{F^{\Gamma_j}(\vec{l},\vec{\xi});\sigma_\nu(\Gamma_k)\}_{\Gamma_i}\ , \tag{D2}$$

where the curly bracket denotes linear combinations of the product $F^{\Gamma_j}(\vec{l},\vec{\xi})$ and $\sigma_\nu(\Gamma_k)$ that transform as Γ_i. In the site representation, the matrix $D^{\Gamma_i}_{XG\pm}(\vec{k})$ assumes the same form as

$D^{\Gamma_i}_{BB'}(\vec{k})$, which is defined by Eqs. (B8) and (B10), subject to the constraint (B12), where $G^{\pm}$, respectively, denotes the graphite layers above (+) and below (−) the intercalate layer. In addition we must in Eq. (B10) replace the Fourier functions $F^{\Gamma_j}(\vec{l},\vec{\xi})$ by $[F_{\Gamma_j}(\vec{l},\vec{\xi}) + F^{\Gamma_j \times B_{2u}}(\vec{l},\vec{\xi})]$ for Γ_j even under time inversion symmetry and by $[F^{\Gamma_j}(\vec{l},\vec{\xi}) - F^{\Gamma_j x B_{2u}}(\vec{l},\vec{\xi})]$ for Γ_j odd.

When expanded to first-neighbor interaction terms within the matrix block D_{GG} (written in the layer representation), the interaction block $D_{XG^{\pm}}$ takes the following forms, depending on whether $G^{\pm}=A'^{\pm}$ or $G^{\pm}=B'^{\pm}$. For $G^{\pm}=A'^{\pm}$, $D_{XG^{\pm}}$ assumes the form

$$D_{XG^{\pm}}=\begin{vmatrix} \delta_{11}^{XG^{\pm}}(\vec{\xi}) & \delta_{12}^{XG^{\pm}}(\vec{\xi}) & \delta_{13}^{XG^{\pm}}(\vec{\xi}) \\ \delta_{12}^{XG^{\pm}*}(\vec{\xi}) & \delta_{22}^{XG^{\pm}}(\vec{\xi}) & \delta_{13}^{XG^{\pm}*}(\vec{\xi}) \\ \delta_{13}^{XG^{\pm}*}(\vec{\xi}) & \delta_{13}^{XG^{\pm}}(\vec{\xi}) & \delta_{33}^{XG^{\pm}}(\vec{\xi}) \end{vmatrix}, \tag{D3}$$

in which the scalar quantities

$$\delta_{11}^{XG^{\pm}}(\vec{\xi})=\sum_l a_{XG}^{A_{1g}}(\vec{l},1)[F^{A_{1g}}(\vec{l},\vec{\xi})\pm F^{A_{2u}}(\vec{l},\vec{\xi})+F^{B_{2u}}(\vec{l},\vec{\xi})\mp F^{B_{1g}}(\vec{l},\vec{\xi})], \tag{D4a}$$

$$\delta_{22}^{XG^{\pm}}(\vec{\xi})=\delta_{11}^{XG^{\pm}}(\vec{\xi}), \tag{D4b}$$

$$\delta_{33}^{XG^{\pm}}(\vec{\xi})=\sum_l a_{XG}^{A_{1g}}(\vec{l},4)[F^{A_{1g}}(\vec{l},\vec{\xi})\pm F^{A_{2u}}(\vec{l},\vec{\xi})+F^{B_{2u}}(\vec{l},\vec{\xi})\mp F^{B_{1g}}(\vec{l},\vec{\xi})], \tag{D4c}$$

$$\delta_{12}^{XG^{\pm}}(\vec{\xi})=\sum_l a_{XG}^{A_{1g}}(\vec{l},3)[F^{E_{2g}}(\vec{l},\vec{\xi})\pm F^{E_{2u}}(\vec{l},\vec{\xi})+F^{E_{1u}}(\vec{l},\vec{\xi})\mp F^{E_{1g}}(\vec{l},\vec{\xi})], \tag{D4d}$$

$$\delta_{13}^{XG^{\pm}}(\vec{\xi})=i\sum_l a_{XG}^{A_{1g}}(\vec{l},5)[F^{E^*_{1g}}(\vec{l},\vec{\xi})\mp F^{E^*_{1u}}(\vec{l},\vec{\xi})-F^{E_{2u}*}(\vec{l},\vec{\xi})\mp F^{E^*_{2g}}(\vec{l},\vec{\xi})], \tag{D4e}$$

and for $G^{\pm}=B'^{\pm}$, we replace l by $-l$ in Eqs. (D4). The nonzero symmetrized Fourier parameters for the XX and XG interactions are given in Table IV.

For stage 1, the above equations become

$$\delta_{ij}^{XG}(\vec{\xi})=\delta_{ij}^{XG^+}(\vec{\xi})+\delta_{ij}^{XG^-}(\vec{\xi}). \tag{D5}$$

*Now at Bell Telephone Laboratories, Murray Hill, N. J.

[1]S. Y. Leung and G. Dresselhaus, Phys. Rev. B (in press).

[2]G. Dresselhaus and S. Y. Leung, Solid State Commun. 35, 819 (1980).

[3]R. J. Nemanich, S. A. Solin, and D. Guérard, Phys. Rev. B 16, 2965 (1977).

[4]J. J. Song, D. D. L. Chung, P. C. Eklund, and M. S. Dresselhaus, Solid State Commun. 20, 1111 (1976).

[5]C. Underhill, S. Y. Leung, G. Dresselhaus, and M. S. Dresselhaus, Solid State Commun. 29, 769 (1979).

[6]S. A. Solin, Mater. Sci. Eng. 31, 153 (1977).

[7]S. Y. Leung, G. Dresselhaus, and M. S. Dresselhaus, Synth. Met. 2, 89 (1980); Solid State Commun. 38, 175 (1981); S. Y. Leung, M. S. Dresselhaus, and G. Dresselhaus, Physica (Utrecht) 105B, 375 (1981).

[8]S. A. Solin, Physica (Utrecht) 99B, 443 (1980).

[9]S. Y. Leung, C. Underhill, G. Dresselhaus, and M. S. Dresselhaus, Solid State Commun. 33, 285 (1980).

[10]P. C. Eklund, G. Dresselhaus, M. S. Dresselhaus, and J. E. Fischer, Phys. Rev. B 16, 3330 (1977).

[11]M. S. Dresselhaus, G. Dresselhaus, P. C. Eklund, and D. D. L. Chung, Mater. Sci. Eng. 31, 141 (1977).

[12]P. C. Eklund and K. R. Subbaswamy, Phys. Rev. B 20, 5157 (1979).

[13]H. Miyazaki, T. Hatano, G. Kusunoki, T. Watanabe, and C. Horie, Physica (Utrecht) 105B, 381 (1981).

[14]N. Caswell and S. A. Solin, Phys. Rev. B 20, 2551 (1979).

[15]P. C. Eklund, N. Kambe, G. Dresselhaus, and M. S. Dresselhaus, Phys. Rev. B 18, 7069 (1978).

[16]W. D. Ellenson, D. Semmingsen, D. Guerard, D. G. Onn, and J. E. Fischer, Mater. Sci. Eng. 31, 137 (1977).

[17]J. Rossat-Mignod, D. Fruchart, M. J. Moran, J. W.

Milliken, and J. E. Fischer, Synth. Met. 2, 143 (1980).
[18]J. D. Axe, C. F. Majkrzak, L. Passell, S. K. Satija, G. Dresselhaus, and H. Mazurek, Extended Abstracts of the Fifteenth Biennial 1981 Carbon Conference, Philadelphia, 1981 (unpublished), p. 52.
[19]A. Magerl and H. Zabel, Phys. Rev. Lett. 46, 444 (1981).
[20]U. Mizutani, T. Kondow, and T. B. Massalski, Phys. Rev. B 17, 3165 (1978).
[21]C. Ayache, E. Bonjour, R. Laguier, and J. E. Fischer, Physica (Utrecht) 99B, 547 (1980).
[22]M. G. Alexander, D. P. Goshorn, and D. G. Onn, Phys. Rev. B 22, 4535 (1980).
[23]C. Horie, M. Maeda, and Y. Kuramoto, Physica (Utrecht) 99B, 430 (1980).
[24]M. Maeda, Y. Kuramoto, and C. Horie, J. Phys. Soc. Jpn. 47, 337 (1979).
[25]S. Y. Leung, G. Dresselhaus, and M. S. Dresselhaus, Solid State Commun. 38, 175 (1981).
[26]L. J. Brillson, E. Burstein, A. A. Maradudin, and T. Stark, in *Proceedings of the International Conference on Semimetals and Narrow Gap Semiconductors, Dallas, Texas, 1970,* edited by D. L. Carter and R. T. Bate (Pergamon, New York, 1971), p. 187.
[27]R. J. Nemanich, G. Lucovsky, and S. A. Solin, Solid State Commun. 23, 117 (1977).
[28]R. J. Nemanich, G. Lucovsky, and S. A. Solin, Mater. Sci. Eng. 31, 157 (1977).
[29]F. Tuinstra and J. F. Koenig, J. Chem. Phys. 53, 1126 (1970).
[30]R. J. Nemanich, G. Lucovsky, and S. A. Solin, in *Proceedings of the International Conference on Lattice Dynamics, Paris, 1975,* edited by M. Balkanski (Flammarion, Paris, 1975), p. 619.
[31]G. Dolling and B. N. Brockhouse, Phys. Rev. 128, 1120 (1962).
[32]R. Nicklow, N. Wakabayashi, and H. G. Smith, Phys. Rev. B 5, 4951 (1972).
[33]A. Yoshimori and Y. Kitano, J. Phys. Soc. Jpn. 2, 352 (1956).
[34]J. A. Young and J. U. Koppel, J. Chem. Phys. 42, 357 (1965).
[35]K. K. Mani and R. Ramani, Phys. Status Solidi B 61, 659 (1974).
[36]A. P. P. Nicolson and D. J. Bacon, J. Phys. C 10, 2295 (1977).
[37]R. J. Nemanich and S. A. Solin, Phys. Rev. B 20, 392 (1979).
[38]A. A. Maradudin, E. W. Montroll, G. H. Weiss, and I. P. Ipatova, *Theory of Lattice Dynamics in the Harmonic Approximation: Second Edition,* Suppl. 3 of *Solid State Physics* (Academic, New York, 1971).
[39]A. Hérold, *Physics and Chemistry of Materials with Layered Structures,* edited by F. Lévy (Reidel, Dordrecht, Holland, 1979), Vol. 6, p. 323.
[40]M. S. Dresselhaus and G. Dresselhaus, in *Physics and Chemistry of Materials with Layered Structures,* edited by F. Lévy (Reidel, Dordrecht, Holland, 1979), Vol. 6, p. 423; Adv. Phys. 30, 139 (1981); in *Light Scattering in Solids,* edited by M. Cardona and G. Güntherodt, (Springer, Berlin, 1981).
[41]D. E. Nixon and G. S. Parry, J. Phys. D 1, 291 (1968).
[42]D. Guérard, C. Zeller, and A. Hérold, C. R. Acad. Sci. Ser. C 283, 437 (1976).
[43]S. Flandrois, J. M. Masson, J. C. Rouillon, J. Gaultier, and C. Hauw, Synth. Met. 3, 195 (1981).
[44]T. Krapchev, M.S. thesis, MIT, 1981 (unpublished).
[45]L. Pietronero and S. Strässler, Proceedings of the 15th International Conference on the Physics of Semiconductors, Kyoto, 1980 [J. Phys. Soc. Jpn. 49, Suppl. A, 895 (1980]; L. Pietronero and S. Strässler, Proceedings of the International Conference on the Physics of Intercalation Compounds, Trieste, Italy, 1981 (in press).
[46]S. Y. Leung, Sc.D. thesis, MIT, 1980 (unpublished).
[47]R. Al-Jishi, B. S. Elman, and G. Dresselhaus, Extended Abstracts of the Fifteenth Biennial Carbon Conference, Philadelphia, 1981 (unpublished), p. 34.
[48]C. W. Lowe, B. S. Elman, G. Dresselhaus, M. S. Dresselhaus, and P. C. Eklund (unpublished).
[49]A. W. Moore, in *Chemistry and Physics of Carbon,* edited by P. L. Walker and P. A. Thrower (Dekker, New York, 1973), Vol. II, p. 69.
[50]A. S. Pine and G. Dresselhaus, Phys. Rev. B 4, 356 (1971).
[51]G. Dresselhaus and M. S. Dresselhaus, Int. J. Quantum Chem. IIS, 333 (1968).
[52]G. Dresselhaus and M. S. Dresselhaus, Phys. Rev. 160, 649 (1967).
[53]L. G. Johnson, Sc.D. thesis, MIT 1973 (unpublished).
[54]A. Magerl and H. Zabel, Proceedings of the International Conference on the Physics of Intercalation Compounds, Trieste, 1981 (in press).
[55]R. Al-Jishi and G. Dresselhaus (unpublished).